Search for parity nonconservation in atomic dysprosium

A. T. Nguyen,[1] D. Budker,[1,2] D. DeMille,[1,*] and M. Zolotorev[3]
[1]*Physics Department, University of California, Berkeley, California 94720-7300*
[2]*Nuclear Science Division, E. O. Lawrence Berkeley National Laboratory, Berkeley, California 94720*
[3]*Center for Beam Physics, E. O. Lawrence Berkeley National Laboratory, Berkeley, California 94720*
(Received 2 June 1997)

Results of a search for parity nonconservation (PNC) in a pair of nearly degenerate opposite-parity states in atomic dysprosium are reported. The sensitivity to PNC mixing is enhanced in this system by the small energy separation between these levels, which can be crossed by applying an external magnetic field. The metastable odd-parity sublevel of the nearly crossed pair is first populated. A rapidly oscillating electric field is applied to mix this level with its even-parity partner. By observing time-resolved quantum beats between these sublevels, we look for interference between the Stark-induced mixing and the much smaller PNC mixing. To guard against possible systematic effects, reversals of the signs of the electric field, the magnetic field, and the decrossing of the sublevels are employed. We report a value of $|H_w| = |2.3 \pm 2.9\ (\text{statistical}) \pm 0.7(\text{systematic})|$ Hz for the magnitude of the weak-interaction matrix element. A detailed discussion is given of the apparatus, data analysis, and systematic effects. [S1050-2947(97)02111-2]

PACS number(s): 32.80.Ys

I. INTRODUCTION

We present here the results of a search for parity nonconservation (PNC) in atomic dysprosium. PNC measurements in atoms provide a test of the standard model and possible extensions to it complementing experiments using high-energy accelerators. Atomic PNC measurements have already reached the experimental precision of 0.35–3 % in several elements [1–4]. The highest precision, recently achieved in cesium [1], also allowed detection of the nuclear-spin-dependent component of atomic PNC, which is induced primarily by the nuclear anapole moment (see Ref. [5] and references therein). Measurements of nuclear-spin-dependent PNC in a variety of atoms would lead to better understanding of nucleon-nucleon weak interactions, particularly the weak meson-nucleon coupling [6].

Dysprosium ($Z=66$) is an attractive system for PNC experiments. There is an enhancement of the PNC mixing caused by the near degeneracy of a pair of opposite-parity levels (both with $J=10$ lying 19 797.96 cm^{-1} above the $J=8$ ground level [7]; see Fig. 1). The magnitude of the level separation is on the order of hyperfine splittings and isotope shift energies. In addition, the existence of many stable isotopes in dysprosium allows for a determination of the weak charge through isotopic comparisons, eliminating the uncertainties associated with atomic calculations [8]. Unfortunately, along with the enhancement of the PNC mixing, there are also factors leading to a reduction of the effect. In particular, the dominant electronic configurations of the nearly degenerate levels are not mixed by the weak interaction and the PNC effect arises from configuration mixing and core polarization.

In this experiment, we look for interference between the PNC and Stark-induced amplitudes connecting the two opposite-parity levels. The value of H_w is extracted from an analysis of the time dependence of fluorescence. With 30 h of integration time, we report the result $|H_w| = |2.3 \pm 2.9(\text{statistical}) \pm 0.7(\text{systematic})|$ Hz (the sign of H_w is the same as the yet undetermined sign of the electric-dipole matrix element). This result is in disagreement with the theoretical prediction of $H_w = 70(40)$ Hz obtained using a multiconfiguration Hartree-Fock-Dirac calculation [9].

In this paper we first give an overview of the experiment, discuss in detail the apparatus and systematic errors, and finally give our results and conclusions.

A. Experimental overview

The spectroscopic properties of the nearly degenerate pair of levels in Dy were investigated in an earlier work [10,11]. The lifetime of the even-parity level (designated as A) is

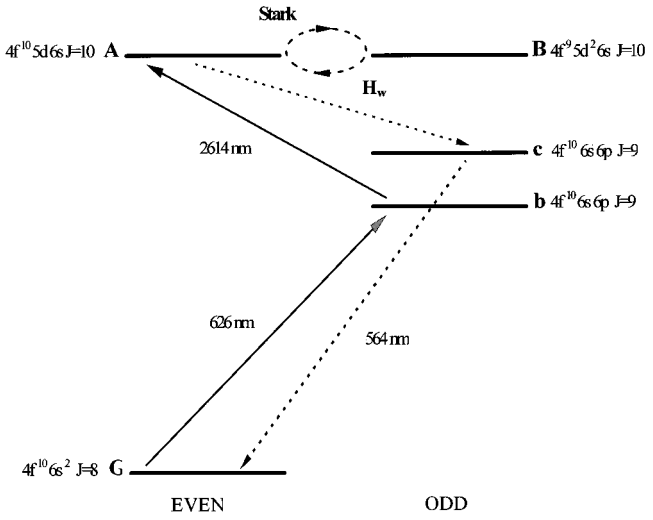

FIG. 1. Partial energy-level diagram of Dy showing PNC and Stark mixing of levels A and B. Solid arrows indicate excitation; dashed arrows indicate fluorescence. Light is detected at 564 nm.

*Present address: Department of Physics, Amherst College, Amherst, MA 01002.

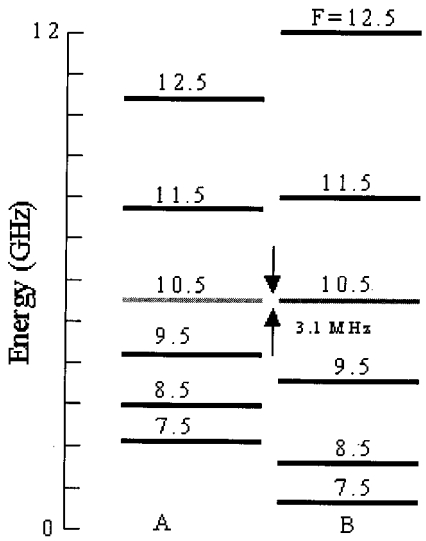

FIG. 2. Hyperfine structure of ^{163}Dy. Zero energy is chosen arbitrarily.

7.9(2) μs. The odd-parity level (designated as B) is much longer lived, with a lifetime greater than 200 μs. Dysprosium has both even and odd nucleon number stable isotopes ($A=156-164$). The two odd nucleon number isotopes ^{161}Dy and ^{163}Dy both have nuclear spin $I=\frac{5}{2}$. The hyperfine components of ^{163}Dy with total angular momentum $F=10.5$ are the closest pair of opposite-parity levels, with a separation of only 3.1 MHz (see Fig. 2). These are the levels used in this experiment. They are connected by the nuclear-spin-independent part of the weak interaction, while the nuclear-spin-dependent contribution to the PNC amplitude is highly suppressed for these particular hyperfine components. This point is discussed in the Appendix.

State A is initially populated by two-step excitation from the ground state using consecutive laser pulses at 626 and 2614 nm, respectively. A magnetic field is applied to bring the sublevels with $|m_F|=10.5$ of A and B nearly to crossing

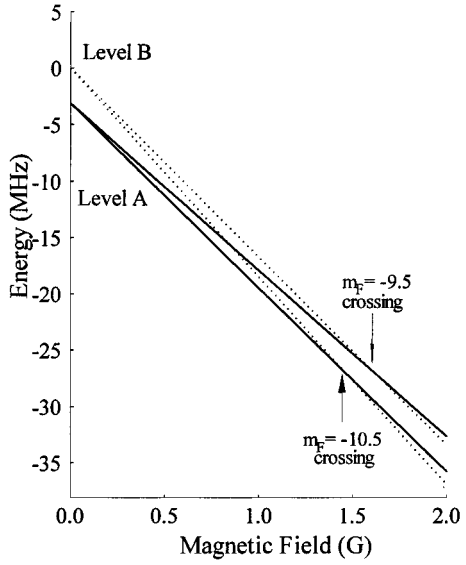

FIG. 3. Partial Zeeman structure of ^{163}Dy $F=10.5$ sublevels of A and B. Zero energy is chosen arbitrarily.

(see Fig. 3), enhancing the PNC mixing between them. An applied electric-field pulse (π pulse) transfers atoms from the nearly crossed Zeeman sublevel of state A to the longer-lived state B.

The PNC and Stark-induced amplitudes have a relative phase of $\pi/2$ (see Sec. I B) and so they do not interfere in a static electric field. In order to achieve interference, a rapidly oscillating (nonadiabatic) sinusoidal electric field is applied parallel to the magnetic field to induce quantum beats between the two opposite parity sublevels. By observing temporal dynamics of the quantum beats, PNC-Stark interference can be detected. A similar scheme of PNC detection was originally proposed for experiments using the $2s$-$2p$ levels in hydrogen [12,13] and was discussed in connection with levels A and B of dysprosium in Ref. [14].

B. PNC-Stark interference

We now describe an analytical model of PNC-Stark interference signal that illuminates the essence of the technique. When the sublevels ($F=10.5$, $|m_F|=10.5$) of A and B are at near crossing (i.e., the energy separation between these sublevels is much smaller than the separation between either of these sublevels and any other sublevel), the Hamiltonian of the system can be simplified to that of a two-level system

$$H=\begin{matrix}\langle A| \\ \langle B|\end{matrix}\begin{pmatrix} -i\Gamma_A/2 & dE+iH_w \\ dE-iH_w & \Delta-i\Gamma_B/2 \end{pmatrix}\begin{matrix} |A\rangle & |B\rangle \end{matrix}. \quad (1)$$

Here $\Gamma_A/2\pi=20$ kHz and $\Gamma_B/2\pi<1$ kHz are the natural widths of A and B, respectively; Δ is the residual energy separation (decrossing), which depends on the applied magnetic field; iH_w is the PNC matrix element (pure imaginary due to T-reversal invariance); E is the applied electric field; and d is the electric-dipole matrix element connecting the sublevels of A and B ($F=10.5$, $m_F=10.5$). The magnitude of this matrix element was experimentally determined to be $|d/2\pi|=3.8(2)$ kHz/(V/cm) [10]. Since dE is real and iH_w is imaginary, interference between these two terms will only occur if E is time varying, with a frequency sufficiently high such that changes in the system are nonadiabatic.

An approximate solution to the Schrödinger equation for the two-level system can be obtained using first-order time-dependent perturbation theory. In the interaction picture the solution has the form

$$|\psi(t)\rangle=c_A(t)|A\rangle e^{-\Gamma_A t/\hbar}+c_B(t)|B\rangle e^{-i\Delta t/\hbar}e^{-\Gamma_B t/\hbar}, \quad (2)$$

which leads to two differential equations for $c_A(t)$ and $c_B(t)$ (in units where $\hbar=1$),

$$\dot{c}_A(t)=-ic_B(t)(dE+iH_w)e^{-i\Omega t}, \quad (3)$$

$$\dot{c}_B(t)=-ic_A(t)(dE-iH_w)e^{+i\Omega t}, \quad (4)$$

where $\Omega=\Delta+i(\Gamma_A-\Gamma_B)/2$. Let $E=E_0\cos(\omega t)$ and let all atoms be in state B at $t=0$. Since $dE_0\ll\omega$ ($\omega/2\pi=100$ kHz) in this experiment, $c_B(t)$ is approximately constant in the time scale of the electric-field oscillation; this allows simple integration of Eq. (3) (first-order perturbation

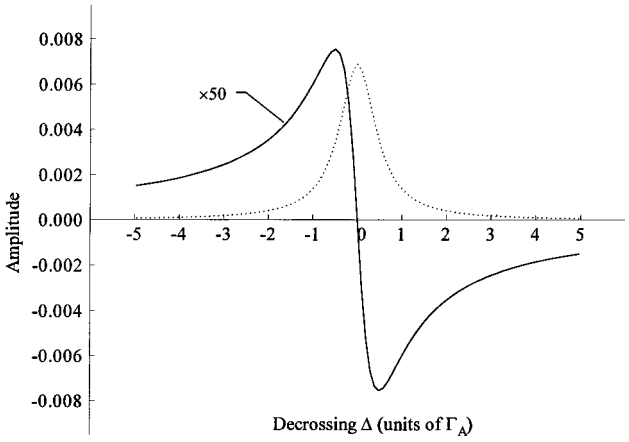

FIG. 4. The solid line shows the calculated PNC-Stark interference term amplitude versus decrossing Δ for $H_w=1$ Hz (for display purposes, this curve has been magnified 50 times). The dashed line shows the calculated interference term amplitude due to a dc electric field ($E_{\rm dc}=60$ mV/cm).

theory). Making the further approximation $\omega \gg |\Omega|$ (again as in the experiment) and only keeping terms of order dE_0/ω and H_w/Ω, we arrive at

$$\langle A|\psi(t)\rangle = c_A(t)e^{-\Gamma_A t/2} = -i\,\frac{dE_0}{\omega}\,e^{-i\Delta t}e^{-\Gamma_B t/2}\sin(\omega t) + iH_w\left[\frac{e^{-i\Delta t}e^{-\Gamma_B t/2}-e^{-\Gamma_A t/2}}{\Omega}\right]. \tag{5}$$

Note that the contribution from second-order perturbation theory is zero because the Stark and PNC interactions are off diagonal in the Hamiltonian [see Eq. (1)].

Returning to Eq. (5), let us consider times t such that $\tau_A = 7.9\ \mu\text{s} \ll t < 200\ \mu\text{s} < \tau_B$. This allows some further approximations, namely, $\Gamma_B \approx 0$ and $e^{-\Gamma_A t} \approx 0$. Thus the population of A is given by

$$|\langle A|\psi(t)\rangle|^2 = \left(\frac{dE_0}{\omega}\right)^2 \sin^2(\omega t) - \frac{2dE_0H_w}{\omega}\left(\frac{\Delta}{\Delta^2+\Gamma_A^2/4}\right)\sin(\omega t). \tag{6}$$

The first term shows the quantum beat signal due to Stark mixing at the second harmonic of the electronic-field frequency. The second term shows interference between H_w and dE_0 at the first harmonic. It changes sign with decrossing (see Fig. 4), the overall sign of the electric field and the magnetic field (the latter reverses the sign of m_F and, correspondingly, that of d). It has the signature of the P-odd, T-even rotational invariant

$$\dot{\mathbf{E}}\cdot(\mathbf{B}-\mathbf{B}_c), \tag{7}$$

where $\mathbf{B}_c$ is the magnetic field required to cross the two sublevels (see Fig. 3). The magnitude of this term is maximal for $|\Delta| = \Gamma_A/2$.

To analyze the current experiment, it is necessary to consider the effects due to a dc electric field ($E_{\rm dc}$) along the direction of B. Such a field, which can easily be included in Eqs. (3) and (4), contributes a term in the population of A with a first-harmonic dependence of the form

$$\frac{2d^2E_0E_{\rm dc}}{\omega}\left(\frac{\Gamma_A/2}{\Delta^2+\Gamma_A^2/4}\right)\sin(\omega t). \tag{8}$$

The amplitude of this interference term has a different signature from PNC since it is even with respect to decrossing (see Fig. 4).

An estimate of the ratio of PNC-Stark interference term to the leading Stark term can be found using Eq. (6). For $\Delta = \Gamma_A/2$, this ratio (denoted as ξ) is

$$\xi = \frac{2\omega H_w}{dE_0\Gamma_A}. \tag{9}$$

In the shot-noise limit, the signal-to-noise ratio is $\xi\sqrt{N}$, where N is the number of detected fluorescence photons due to atoms decaying from state A:

$$N \sim N_0\left(\frac{d^2E_0^2}{\omega^2}\right)\Gamma_A T \leqslant N_0. \tag{10}$$

Here N_0 is the original number of atoms and T is the transit time of the atoms through the interaction and detection region. Thus the signal-to-noise ratio is

$$2H_w\sqrt{\frac{T}{\Gamma_A}}\sqrt{N_0}. \tag{11}$$

Although T can be large, it is ultimately limited by the lifetime of B, at which point the signal-to-noise ratio becomes $(2H_w/\sqrt{\Gamma_A\Gamma_B})\sqrt{N_0}$. Note that because we are able to set the decrossing Δ to its optimum value, the final signal-to-noise ratio does not depend on the initial level separation; this is a situation radically different from that in traditional PNC experiments.

II. APPARATUS

The following sections describe the atomic-beam apparatus, the optical setup, the electric and magnetic fields, and the detection system (see Figs. 5 and 6).

A. Atomic beam

The atomic-beam source was an effusive oven with a multislit nozzle array. The oven body was constructed from molybdenum tubing of outer diameter 2.54 cm, wall thickness 0.1 cm, and length 6.4 cm. End caps made of tantalum were tied with tantalum wire to either end of the tube. An array of slits on one of the end caps was made using a wire electrical discharge machine. The use of a slit pattern reduces off-axis beam flux and thus the overall material consumption. The opening of each slit was $0.04\times0.5\ \text{cm}^2$ with a depth of 0.6 cm. These dimensions were chosen to give the same beam divergence angle ($\sim 6°$) as provided by the atomic-beam collimators (see Figs. 5 and 6). There were 25 slits, making the total overall area of the array of $\sim 1.3\times0.5\ \text{cm}^2$. Dysprosium was loaded through a 1-cm-diam

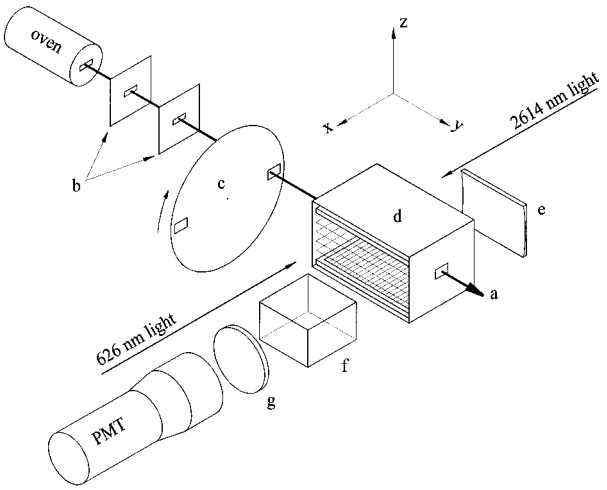

FIG. 5. Schematic view of the apparatus (not to scale): (a) atomic beam; (b) collimators; (c) atomic beam chopper; (d) interaction region of atoms with electric and magnetic fields, with the entire region enclosed in a magnetic shield (not shown), (e) mirror (other mirrors are installed above and below the E-field wire grids); (f) light pipe; and (g) interference filter.

hole made in the opposite end cap. A piece of Ta sheet was press fitted to this hole in order to seal it.

Resistive heaters, made from coiled tantalum wire and held in high-purity alumina ceramic tubes, surrounded the oven. To guard against dysprosium condensation at the slits, the heaters extended past the exit orifice by 3.6 cm. In addition, a fraction of the heaters were $\sim 50\%$ shorter in the back of the oven, which allowed for overheating of the front (typically maintained 100 K hotter than the back). Five layers of tantalum radiation shielding surrounded the heaters and oven.

The oven typically operated at a temperature of 1500 K, which corresponds to a Dy vapor pressure of $\sim 10^{-1}$ Torr. The material output of the oven was ~ 0.6 g/h. Using laser absorption measurements, it was determined that the beam density was $\sim 10^{10}$ atoms/cm^3 at the laser–atomic-beam interaction region, in agreement with estimates based on effusive flow from the slits.

After passing through collimators, the atomic beam encountered a chopper wheel (see Figs. 5 and 6), which was used to block oven blackbody radiation. The anodized aluminum wheel was 13 cm in diameter and had two slits, each with area 2.0×0.8 cm^2, which allowed passage of the atomic beam. The water-cooled chopper wheel motor drive was placed inside the vacuum chamber. The wheel rotated at 230 rps. A sensor of its angular position (a light-emitting diode and a photodiode) was used for triggering of the laser pulses, the electric-field sequence, and detection electronics.

B. Lasers and optics

Pulsed laser light with wavelengths of 626 and 2614 nm was used in the experiment (see Fig. 7). The laser system was described in detail elsewhere [10]. In order to produce 626-nm light, a pulsed dye amplifier (PDA) with DCM [4-Dicyanmethylene-2-methyl-6-(*p*-dimethylaminostyryl)-4H-pyran] dye was used. The PDA was pumped by a Quanta Ray DCR-2 Nd:YAG laser (where YAG denotes yttrium aluminum garnet) and seeded with ~ 100 mW of 626-nm cw light produced by a dye laser (Coherent CR599-21) operating with Rhodamine 590 or DCM dye. Typical PDA output pulses had an energy of ~ 3 mJ, a duration of ~ 7 ns, a beam diameter of ~ 3 mm, and a repetition rate of 10 Hz. A portion of this light was split off and directed to the vacuum chamber. This 626-nm light was attenuated to ~ 10 μJ/pulse in order to saturate only the desired hyperfine components (see below).

2614-nm light was produced by nonlinear mixing (in a 3.5-cm $MgO:LiNbO_3$ crystal) of the remainder of the 626-nm light and light at 823 nm. The 823-nm light was produced by a pulsed dye laser (Quanta Ray PDL-2), pumped by a second Nd:YAG laser. The typical pulse energy for the 2614-nm light was ~ 5 μJ. In order to stabilize the output power, the crystal was placed inside a thermally insulated housing that was temperature stabilized to within 0.5 K with a thermoelectric element. The residual 626- and 823-nm light was filtered from the 2614-nm light by a 0.05-cm-thick Si plate.

State A ($J=10$) was populated by two $\Delta J=+1$ transitions from the ground state ($J=8$) via an intermediate state ($J=9$) (see Fig. 1). In general, the $\Delta F=\Delta J=+1$ transitions are the strongest (see [15] for a discussion). Thus, in order to populate $F=10.5$, $|m_F|=10.5$ sublevels of state A, it was necessary to efficiently transfer atoms initially in the F

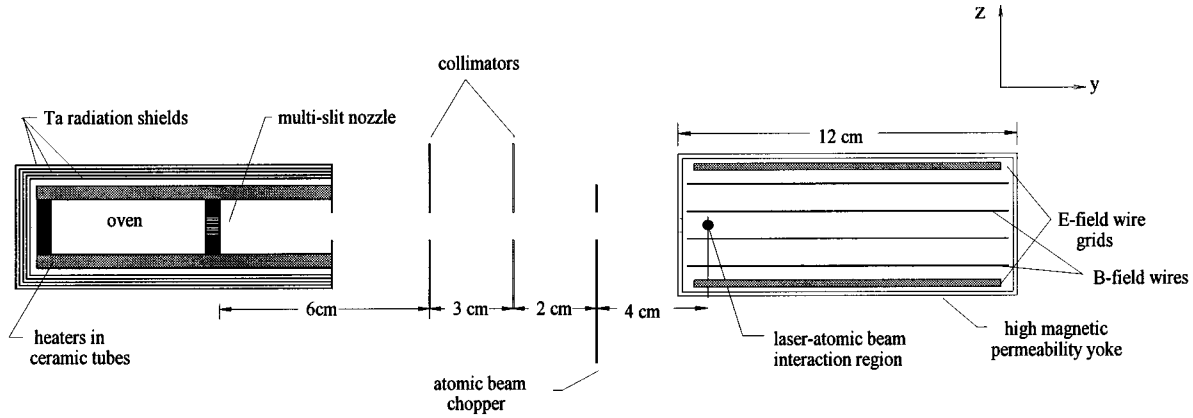

FIG. 6. Side cross-sectional view of the oven and the electric- and magnetic-field interaction region (not to scale). E-field wires with distributed potential (see Sec. II C) are not shown.

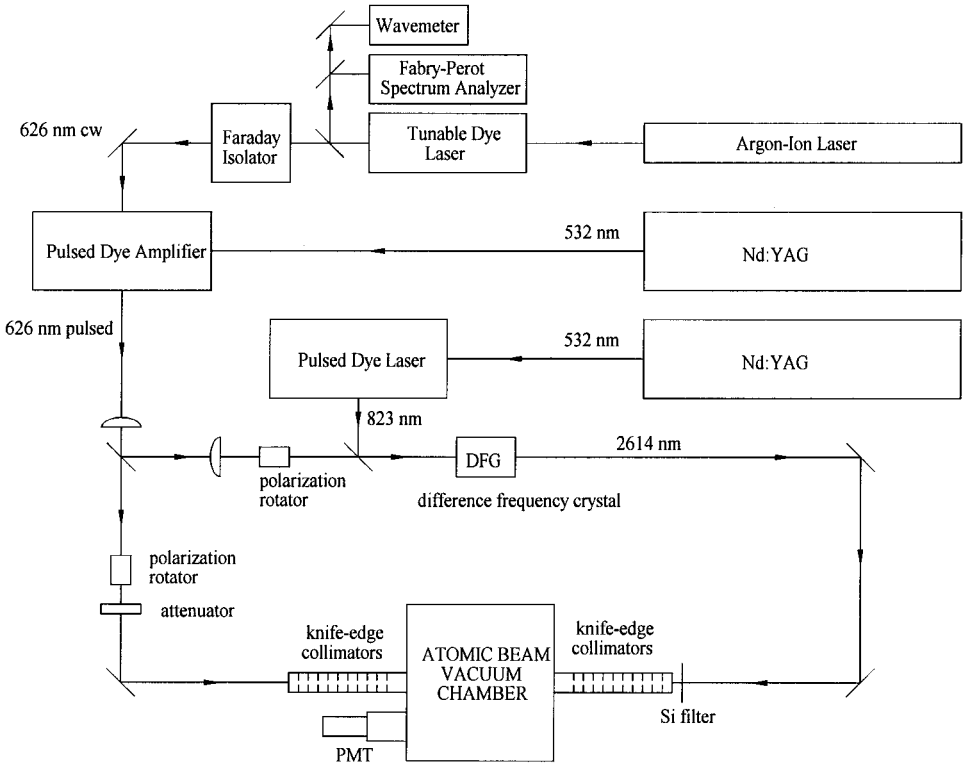

FIG. 7. Diagram of the optical setup.

$=8.5$, $|m_F|=8.5$ sublevels of the ground state by maximizing the probability of $|\Delta m_F|=+1$ transitions. This was achieved with 626-nm and 2614-nm light linearly polarized in the $\hat{y}$ direction, perpendicular to the electric and magnetic fields. Both laser beams passed through collimating lenses before entering the vacuum chamber. Knife-edge collimators placed inside the vacuum chamber between the input windows and the laser–atomic-beam interaction region were used to reduce scattered light (see Fig. 7).

Mirrors surrounding the electric- and magnetic-field interaction region directed fluorescent light towards a lucite light pipe. Light was detected with a 7.6-cm-diam photomultiplier tube (PMT) (Philips XP 3461B) placed outside the vacuum chamber behind the light pipe. The input window of the PMT was covered with a custom designed 564-nm interference filter (CVI Laser Corp.), which had an acceptance angle of 45°. The laser–atomic-beam interaction region was not directly visible to the PMT. Nevertheless, a substantial signal arose both from residual scattered light due to the excitation laser pulses and from the initial fluorescence from state A (due to atoms not transferred to state B). Because of this, a gating circuit was utilized in order to avoid saturation of the PMT. This was accomplished by applying -300 V to the accelerating grid electrode of the PMT for a period of 50 μs during and following the initial population of state A. The anode of the PMT was terminated into a 10-kΩ resistor. The voltage across this resistor was recorded with a digital oscilloscope (Tektronix TDS 410A). The RC time of the detection system was 0.79 μs.

C. Electric and magnetic fields

The electric field was formed between two wire grids (5.6×10.4 cm^2 each) (see Fig. 6). Wire grids were used in order to minimize surface area and thus stray electric charge accumulation. They were constructed by winding 50-μm-(0.002-in.-) diam Be-Cu wire around brass frames with the ends of the wires held tight by screws. There were altogether 40 wires per frame, with a 2.5-mm separation between adjacent wires. The average separation between the two grids was 2.588 cm, with a variation of less than 0.005 cm across the grid area.

In order to achieve a high level of electric-field homogeneity near the grid fringes, four additional wires (50-μm-diam Be-Cu) were wrapped adjacent to the magnetic field wires. A resistive voltage divider distributed the potential among these wires. Using computer modeling [16], an optimum resistor configuration was found, which produced a calculated fractional inhomogeneity of $\lesssim 5\times 10^{-4}$ over the volume occupied by the atomic beam. In addition, the modeling showed that electric field at the center was smaller by 20% relative to what would be expected from infinite, solid plane electrodes.

The magnetic field was produced by eight turns of gold plated copper wire (0.05 cm in diameter) surrounding the electric-field region. The separation between the wires was 0.6 cm. This separation allowed for maximal light detection and sufficient magnetic-field homogeneity. The wires were wound in a pattern minimizing components perpendicular to the electric field. A precision current regulator provided a current stable to 50 μA (corresponding to a magnetic-field stability at a level of 1 mG). High homogeneity of the magnetic field was achieved by providing a yoke for the return of magnetic flux lines. The yoke was made of 2.5-mm-thick high-permeability magnetic material (CO-NETIC AA [17]). In order to shield against laboratory magnetic fields, a 0.76-mm-(0.030-in.-) thick CO-NETIC shield surrounded the en-

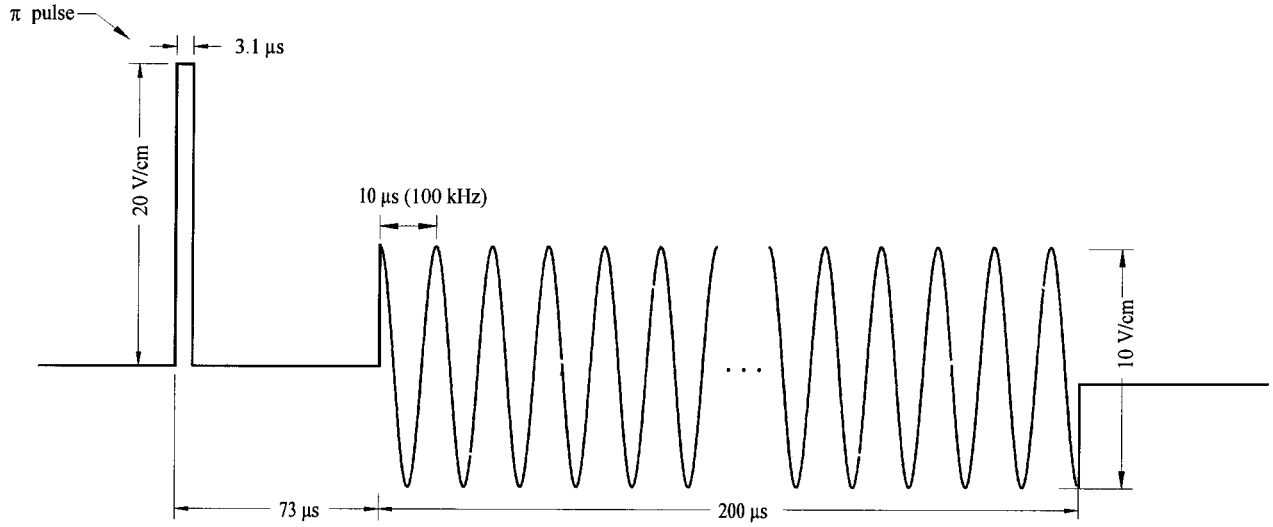

FIG. 8. Electric-field sequence used in the PNC experiment. E-field reversal is achieved by changing the overall sign of this sequence.

tire region. The yoke also provided shielding from external magnetic fields. The fractional variation in the magnitude of the magnetic field was measured to be $\lesssim 10^{-3}$ over an 8 cm length along the volume occupied by the atomic beam. Average fields strengths of up to 2 G were achieved within the volume of the magnetic field region (300 cm^3). All metal parts in the electric- and magnetic-field region were gold plated. This was done to minimize possible stray charge accumulation by dielectric films formed on the surface (see, e.g., Ref. [18]). In addition, it guards against the presence of stray magnetic fields due to thermoelectric currents resulting from the junction of dissimilar metals [19].

III. PNC-STARK INTERFERENCE MEASUREMENT

This section describes the details of data collection and the method of analysis used to arrive at a value for H_w. Figure 8 shows the electric-field sequence with parameters used in the PNC experiment. It was programmed into an arbitrary wave-form generator (Stanford Research Systems DS345), which was output to an amplifier. To remove slow dc offsets in the electric field, a capacitor was placed in series at the output of the amplifier. The initial square π pulse transferred atoms from state A to state B. The parameters of the π pulse were chosen to maximize the number of atoms transferred to the $|m_F|=10.5$ sublevels while minimizing that for $|m_F|=9.5$ sublevels. The sinusoidal electric field ($\sim$5-V/cm amplitude) was applied after a time delay ($\approx 70\ \mu$s), giving sufficient time for atoms remaining in state A (in all sublevels) to decay (recall that $\tau_A=7.9\ \mu$s). In addition, during this time, atoms that were in the laser interaction region (which is not visible to the PMT) during the population pulse have moved into the field of view of the light detection system (see Figs. 5 and 6). As discussed in Sec. I B, the frequency of the sinusoidal electric field (100 kHz) was chosen to be greater than any other relevant frequency scale (i.e., Γ_A, Δ, or dE_0). The initial phase of the sinusoidal wave was chosen to minimize transient effects due to atoms rapidly transferred to state A at the beginning of the wave. The laser pulses, electric-field sequence, PMT gating, and oscilloscope triggering were synchronized to the atomic-beam chopper.

To guard against various systematic effects, data were taken at different values of the decrossing: $\Delta \simeq -\Gamma_A$, 0, and Γ_A, corresponding to $|B| \approx 1.452$, 1.462, and 1.472 G, respectively. Data were also taken with both signs of both the electric and magnetic fields (both signs of $|m_F|=10.5$). Here and throughout, electric-field reversal is taken to mean an overall sign change of the sinusoidal wave and the π pulse. A typical data ''run'' corresponds to a few hours of data taking. Data recorded in a run consists of a series of ''files.'' One file contains four ''channels'' corresponding to the four combinations of the signs of electric and magnetic fields: (1) E_+, B_+; (2) E_-, B_+; (3) E_+, B_-; and (4) E_-, B_-. Data in each channel are the average of fluorescence wave forms from 200 consecutive laser pulses. Averaging was done using an internal function of the digital oscilloscope. It takes approximately 80 s in real time to produce one file.

A. Preliminary considerations

In order to analyze the data, it is necessary to account for several imperfections in the apparatus. In particular, it is necessary to measure the time-dependent efficiency of light detection and backgrounds. The light detection efficiency depends largely upon the geometrical incidence angle of fluorescence light on the detection system (light pipe, interference filter, and PMT; see Fig. 5) averaged over the spatial distribution of the fluorescing atoms. It was measured by using two consecutive π pulses of the electric field, separated in time. Following the usual population of state A, the first pulse transfers atoms to state B; the second transfers them back to state A and fluorescence is detected. Varying the time interval between the two pulses reproduces the actual temporal distribution of the detection efficiency in the PNC experiment. Figure 9 shows a typical normalized light detection efficiency curve. It was verified that this curve remained relatively constant throughout a run. Efficiency data were taken before every run and fitted to a fifth-order polynomial $\mathcal{E}(t)$.

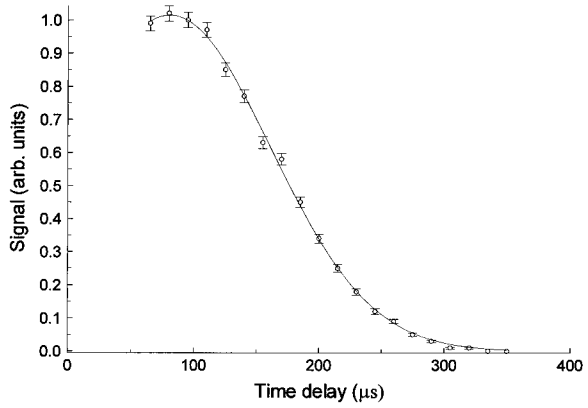

FIG. 9. Efficiency $\mathcal{E}(t)$ of the light detection system as a function of time delay between two π pulses. Points, data; solid curve, curve fit used in data analysis.

Three to four sets of background files were taken within a run. Background data consist of two files: without laser light (B_1) and with laser light but without an electric-field sequence (B_0). The primary contribution to B_1 is due to electronic background from the PMT gating circuit. By taking the difference between B_0 and B_1, we arrive at background due entirely to laser light (B_2). Figure 10 shows typical background data. B_1 was fitted to a fifth-order polynomial, while B_2 was fitted to a simple exponential curve.

Figure 11 shows typical fluorescence data from one channel. Both B_1 and B_2 contribute to the signal. There are 500 points in a 200-μs interval. For data analysis, estimated shot-noise error bars are assigned to each point. However, adjacent points are correlated due to the finite integration time of the detection system. Therefore, the number of degrees of freedom N in a fit is $\sim$150. The data are fitted to a function of the form

$$S_{\rm fit}(t)=\alpha_1+B_1(t)+\alpha_2 B_2(t)+\alpha_3\mathcal{E}(t)f(E,\Delta,H_w;t), \tag{12}$$

where α_1, α_2, α_3, E, Δ, and H_w are free parameters. The parameter α_1 is included to account for slowly varying overall offsets. The function $f(E,\Delta,H_w;t)$ is the fluorescence line shape obtained by numerical integration of the Schrödinger equation with appropriate E, Δ, and H_w, with the finite integration time of the detection system (0.79 μs) and lifetime of the intermediate state (2.2 μs) included. E and Δ are free parameters because we allow for imperfect E and B fields (see Sec. III B).

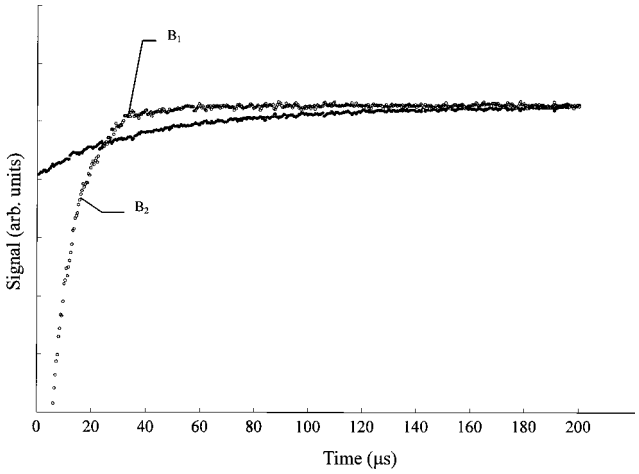

FIG. 10. Background data: B_1, background independent of laser light; B_2, background due to laser light.

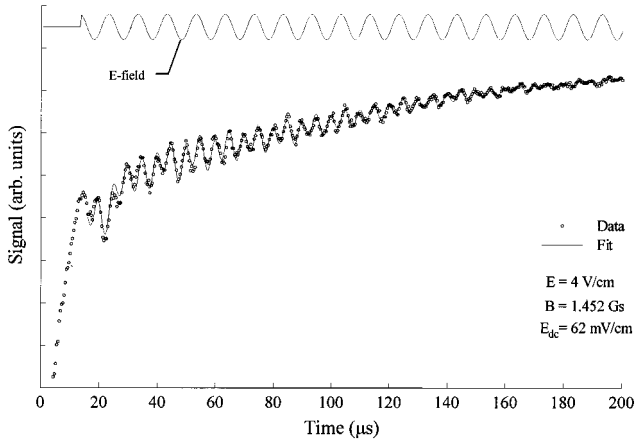

FIG. 11. Typical data from a given channel. Best-fit values for β and $E_{\rm dc}$ have been used for the shown fit. The first-harmonic term due to $E_{\rm dc}$ can readily be seen. Each point corresponds to an average over 200 laser shots ($\sim$20 s of real time). Also the cosine E field has been superimposed for purpose of display. The vertical scale is the same as in Fig. 10.

By considering only that part of the signal that occurs before the electric-field sequence ($t<15$ μs), α_1 and α_2 are determined first for each data channel. Thus the remainder of the signal must be fitted to four free parameters. Such a fit requires extensive computation since the fluorescence line shape $f(E,\Delta,H_w;t)$ must be calculated for each change in E, Δ, or H_w. To avoid this, a procedure that relies upon the signatures of both $E_{\rm dc}$ and H_w (see Fig. 4) was developed. We will now present this procedure and discuss various checks of its validity.

B. Fitting the magnetic field and electric field

The first step in the fitting procedure is to determine the magnetic-field calibration and to determine dc components of the electric field. [Note that throughout the fitting procedure, for a specific $f(E,\Delta,H_w;t)$, α_3 is fitted automatically using a least-squares method.]

In Sec. I B, it was shown that Stark-PNC interference leads to a component of the signal at the first harmonic of the oscillating electric field frequency. A dc electric field applied in addition to the oscillating electric field also causes a similar component [see Eq. (8)]. However, the PNC component can be distinguished from the component due to the dc electric field since the former is an odd function of Δ while the latter is even (see Fig. 4). As an important note, we only need to consider z components of the electric and magnetic fields. Although other components would tend to mix in a contribution from the $|m_F|=9.5$ sublevel, this contribution is negligible due to the large energy separation ($\sim$300 kHz) and the smaller dipole matrix element connecting it to the $|m_F|=10.5$ sublevel.

There are two types of dc electric field ($E_{\rm dc}$) to consider: one that reverses sign with reversal of the electric-field sequence, $E_{\rm dc}$(odd), and one that does not, $E_{\rm dc}$(even). The latter is mainly attributed to surface charge accumulation on the electric-field wires. Even after the wires were gold plated (see Sec. II C), fields of up to ~ 80 mV/cm were produced within a few months of operation. The other type of dc electric field, $E_{\rm dc}$(odd), allows for imperfect reversal of the electric-field sequence by the amplifier. For each run, we first found the best fits to both types of dc electric field before fitting the value of H_w. The value of electric field used in the fit was

$$E_{\rm fit}(t) = E_{\rm applied}(t) + E_{\rm dc}({\rm odd}) + E_{\rm dc}({\rm even}). \tag{13}$$

Note that in the numerical calculations used for data analysis, it was important to assume that $E_{\rm dc}$ interacts with atoms at all times after the electric-field π pulse. This produces an effective ''premixing'' of A and B prior to application of the sinusoidal electric field, which slightly modifies the initial transients in the fluorescence line shape.

Let us now discuss calibration of the magnetic field. It is possible to calibrate the magnetic field using the data. Allowing for an imperfect reversal of magnetic coil current and small residual magnetic-field offsets, separate calibration constants β_+ and β_- were used corresponding to nominal magnetic field in the $+\hat{z}$ direction (B_+) and the $-\hat{z}$ direction (B_-), respectively:

$$B_{\rm fit+} = \beta_+ B_+ , \tag{14}$$

$$B_{\rm fit-} = \beta_- B_- , \tag{15}$$

where $B_{\rm fit+(-)}$ refers to the value of the magnetic field used in the fit.

To fit for $E_{\rm dc}$ and β, we first set $H_w = 0$ (the validity of this step will be discussed below). We next generated a two-dimensional map of reduced χ^2 values of the fit as a function of both $E_{\rm dc}$ and β. Typical maps are shown for an on-crossing ($\Delta = 0$) file and an off-crossing ($\Delta \sim \Gamma_A$) file in Figs. 12(a) and 12(b), respectively. The contours correspond to constant levels of reduced χ^2, while the minimum of χ^2 ($\chi^2_{\rm min}$) corresponds to the best-fit values for $E_{\rm dc}$ and β. As expected, $\chi^2_{\rm min}$ approximately equals unity. For a two-parameter fit, choosing the contour that is $2.3/N$ away from $\chi^2_{\rm min}$ (where $N \approx 150$ is the number of degrees of freedom) will give a 68% confidence level in the choice of parameters within the contour (see, e.g., [20] for a detailed discussion).

All χ^2 maps of a particular channel were averaged together resulting in four maps (one per channel) for each run. This was done in order to combine information in the on- and off-crossing maps. The uncertainty of a parameter for a particular channel is determined by taking the projection of the resulting contour onto the parameter's axis.

$E_{\rm dc}$(even) and $E_{\rm dc}$(odd) are found by taking the weighted average of the four values of $E_{\rm dc}$ (with appropriate signs) from each data channel. From run to run, $E_{\rm dc}$(even) varied from 0 to 80 mV/cm, while $E_{\rm dc}$(odd) remained a constant $\approx -4(1)$ mV/cm (the negative sign indicates polarity opposite to the electric-field π pulse). A contribution to $E_{\rm dc}$(odd) comes from discharge of the capacitor, which removes slow dc offsets from the amplifier output. This capacitor is initially charged by the electric-field π pulse. The corresponding field was calculated to be -5 mV/cm. Thus $E_{\rm dc}$(odd) attributed to imperfect reversal of the electric field sequence is 1(1) mV/cm. This procedure to determine $E_{\rm dc}$ was checked by deliberately applying several values of dc electric field. The fitted values for $E_{\rm dc}$ were in agreement with the applied values. Finally, the calibration constants $\beta+$ and $\beta-$ were found to be within $\approx 0.2\%$ of each other.

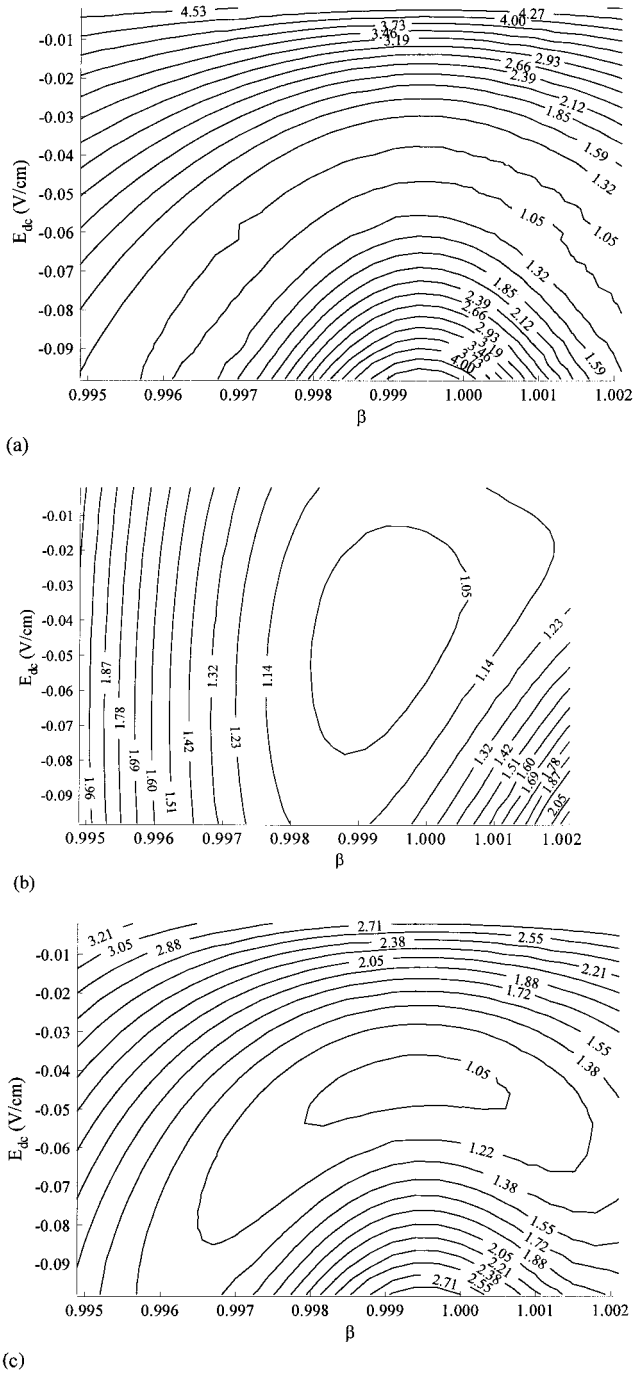

FIG. 12. Fitting $E_{\rm dc}$ and β. Contour maps show constant levels of reduced χ^2 for (a) an on-crossing file, (b) an off-crossing file, and (c) the average of the two.

TABLE I. Summary of sign change in fitted H_w under reversal of E, B, or Δ for PNC effect and imperfections.

PNC effect and imperfections	Reversal E	B	Δ
PNC	+	+	+
$\partial E_{dc}/\partial x$ (E even)	+	−	−
$\Delta E_{dc}/\partial x$ (E odd)	−	−	−
$\partial B/\partial x$ (B even)	−	+	−
$\partial B/\partial x$ (B odd)	−	−	−
$E_{dc}\partial B/\partial x$ (E even, B even)	+	+	+
$E_{dc}\partial B/\partial x$ (E odd, B even)	−	+	+
$E_{dc}\partial B/\partial x$ (E even, B odd)	+	−	+
$E_{dc}\partial B/\partial x$ (E odd, B odd)	−	−	+
$(\partial E_{dc}/\partial x)(\partial B/\partial x)$ (E even, B even)	+	+	+
$(\partial E_{dc}/\partial x)(\partial B/\partial x)$ (E odd, B even)	−	+	+
$(\partial E_{dc}/\partial x)(\partial B/\partial x)$ (E even, B odd)	+	−	+
$(\partial E_{dc}/\partial x)(\partial B/\partial x)$ (E odd, B odd)	−	−	+
$(\partial B/\partial x)B_0$ (B even)	−	+	−
$(\partial B/\partial x)B_0$ (B odd)	−	−	−

C. Fitting H_w

With the values of E_{fit} and B_{fit} fixed for a specific channel, the value for H_w was fitted. Only off-crossing files ($|\Delta| = \Gamma_A$) were considered since the Stark-PNC interference term at crossing is zero (see Fig. 4). χ^2 as a function of H_w was generated. For a one-parameter fit, the uncertainty in H_w was estimated by determining the values of H_w that change χ^2_{min} by $1/N$. The uncertainty in H_w obtained in this way was consistent with the spread of the values between different files. The final value of H_w is the weighted average from all channels of all files.

As discussed above, the value of H_w is initially set to zero in the fitting procedure. However, it was found by fitting computer-generated simulated data that this procedure results in a difference between the input value of H_w and the resulting fitted value by a multiplicative factor slightly different from unity. This is because, if H_w is nonzero, its noninclusion in the initial fit for E_{dc} and β leads to a correction in the fitted values of these parameters; this in turn results in a normalization factor for the final value of H_w. Computer modeling shows that the actual value of H_w is obtained by multiplying the fitted value by 1.3.

To additionally verify the data analysis procedure, χ^2 three-dimensional maps with coordinates representing all three parameters (E_{dc}, β, and H_w) were made for several files. The confidence region, in this case, is an ellipsoid in parameter space. It was found that the central value and uncertainty of these parameters agreed well with those obtained by the procedure described.

IV. SYSTEMATIC EFFECTS

In principle, it is possible that certain combinations of imperfections involving electric- and magnetic-field gradients in the system could mimic the signature of the PNC effect. We considered four imperfections: a residual magnetic field B_0, a dc electric field E_{dc}, and their gradients

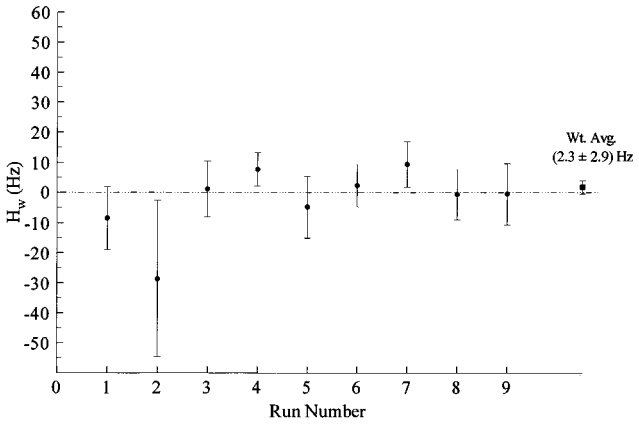

FIG. 13. Summary of PNC data.

$\partial B/\partial x$ and $\partial E_{dc}/\partial x$, respectively. By separately fitting E_{dc} to the beginning and to the end of the fluorescence data, $\partial E_{dc}/\partial x$ was found to be $\leqslant 3$ mV/cm/cm.

The imperfections are allowed to be either even or odd with respect to the reversal of E or B. Simulated data that included these imperfections were generated. In order to determine whether a given combination of imperfections has a signature mimicking H_w, we fitted these data with a fluorescence line shape allowing variation of H_w (but not of E_{dc} and β, which were set to 0 and 1, respectively). By reversing E, B, and Δ, we determined whether or not the sign of the fitted value of H_w changed. This allowed us to rule out the combinations of imperfections that did not have the same signature as PNC. Table I shows the various combinations of at most two imperfections and the corresponding signatures of the fitted value for H_w. A systematic effect that mimics the PNC effect would be one in which the sign of the fitted H_w does not change sign under reversals of E, B, and Δ.

From Table I, there are two potentially dangerous combinations of imperfections: $E_{dc}\partial B/\partial x$ (E even, B even) and $(\partial E_{dc}/\partial x)(\partial B/\partial x)$ (E even, B even). To see what value of false H_w corresponded to these effects, we once again generated simulated data that included these imperfections. This time, however, the complete fitting procedure described in Sec. III was applied to the simulated data. Using the mea-

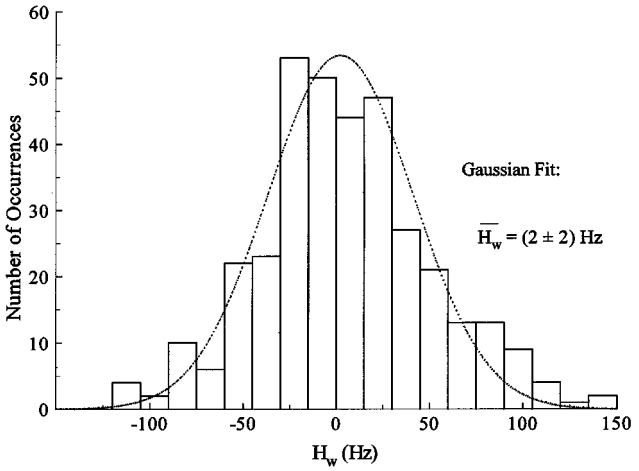

FIG. 14. Histogram of fitted H_w for each individual file. The smooth curve is a best-fit Gaussian.

TABLE II. Fitted values of H_w grouped according to channels and to decrossing Δ.

	Channel 1 (E_+B_+)	Channel 2 (E_-B_+)	Channel 3 (E_+B_-)	Channel 4 (E_-B_-)	$\Delta<0$	$\Delta>0$
H_w (Hz)→	-0.9 ± 5.6	-1.0 ± 5.7	0.5 ± 5.5	10.9 ± 5.6	0.1 ± 3.5	9.4 ± 4.9

sured value of $\partial B/\partial x$ and the estimate for $\partial E_{\rm dc}/\partial x$, it was found that these effects produced a false $|H_w|\leq 0.7$ Hz. This value provides an upper limit of the systematic errors. As an additional test for systematic effects, we have checked for a dependence of the fitted values of H_w upon $E_{\rm dc}$. No such dependence was found within statistical uncertainties.

V. RESULTS AND CONCLUSIONS

Figure 13 shows the values for H_w obtained from run to run. Figure 14 shows a histogram of fitted H_w from all channels along with a best-fit Gaussian. Data grouped according to channels and according to decrossing Δ are shown in Table II. No statistically significant discrepancies are observed. Finally, we report a value for $|H_w|=|2.3\pm2.9(\text{statistical})\pm0.7(\text{systematic})|$ Hz (here the normalization factor discussed in Sec. III C has been accounted for). The sign of the central value of H_w is the same as that of the electric-dipole matrix element d.

As mentioned earlier, the theoretical prediction for the nuclear-spin-independent weak matrix element is $H_w=70(40)$ Hz [9]. A cancellation between the nuclear-spin-dependent (NSD) and spin-independent contributions is unlikely because $F=10.5$ hyperfine components are insensitive to NSD effects (see the Appendix).

For the future, there are several planned improvements to increase experimental sensitivity. Another order of magnitude in counting rate is possible if one uses optical pumping to concentrate the population into one Zeeman sublevel of the ground state. An even greater improvement would be achieved by switching to cw lasers for excitation. A 100% duty cycle would allow three to four orders of magnitude increase in counting rate. A cw scheme to populate state B is currently being investigated. These improvements should allow for a statistical sensitivity of ~1 mHz in one month of data taking. If the magnitude of H_w is $\sim1-3$ Hz, this level of sensitivity will be sufficient for testing the standard model and for measurement of nuclear-spin-dependent effects (see the Appendix).

ACKNOWLEDGMENTS

We are grateful to E. D. Commins for his significant contributions to this work in its early stages and for helpful discussions; C. J. Bowers, V. V. Flambaum, I. B. Khriplovich, M. Kozlov, M. Lintz, B. C. Regan, and O. P. Sushkov for valuable discussions; machinist A. Vaynberg and electronics engineers J. Davis and D. Gallegos for their excellent work; and Lars Commins for technical assistance. This research has been supported by the National Science Foundation under Grant No. PHY-9311610 and by University of California, Berkeley COR Faculty and Junior Faculty Research Grants.

APPENDIX: NUCLEAR-SPIN-DEPENDENT PNC EFFECTS

In this appendix we briefly consider nuclear-spin-dependent PNC effects and determine the relative sensitivity of quantum-beat experiments involving various hyperfine components of the states A and B. The NSD PNC effect is generally expected to be at a few percent level of the dominant contribution [5].

For the matrix element of the NSD PNC [5] we have

$$\hat{H}_{\rm NSD}\propto iZ^2R\kappa\mathbf{I}\cdot\mathbf{J}, \tag{A1}$$

where R is a relativistic factor and κ is the effective coupling constant, which includes contributions from standard model vector hadronic and axial electronic current coupling, as well as that of the nuclear anapole moment. Since $\hat{H}_{\rm NSD}$ is a scalar operator, it is nonzero only for components of A and B with the same values of F and m_F. However, the matrix element of $\hat{H}_{\rm NSD}$ is different for different relative orientations of total electronic angular momentum and nuclear spin, i.e., for different values of F. Since states A and B have the same total electronic angular momentum ($J=10$), evaluation of the angular part of $\hat{H}_{\rm NSD}$ is equivalent to taking the diagonal matrix element of the operator $\mathbf{I}\cdot\mathbf{J}$:

$$\langle\hat{H}_{\rm NSD}\rangle\propto\tfrac{1}{2}[F(F+1)-J(J+1)-I(I+1)]. \tag{A2}$$

(Note that the NSD PNC matrix element is proportional to magnetic-dipole hyperfine-structure shift for a given F component.) Evaluating $\langle\hat{H}_{\rm NSD}\rangle$ for different values of F (with $J=10$ and $I=\frac{5}{2}$, which is the case for both stable odd nucleon-number isotopes ^{161,163}Dy), one finds that the maximum absolute values of the numerical factor (-27.5 and 25.0) are obtained for the extreme values $F=7.5$ and 12.5, respectively, while the smallest (1.0) is obtained for $F=10.5$. Therefore, the $F=10.5$ components used in the present experiment are least sensitive to NSD PNC.

Since a relatively high NSD PNC contribution for this particular system (states A and B) was predicted in [9] (at the level of $\sim20\%$ of the dominant nuclear-spin-independent effect) and the dominant contribution was found to be suppressed compared to the calculated value, one could imagine a cancellation involving the NSD and nuclear-spin-independent contribution for some hyperfine components. For the $F=10.5$ components used in the present experiment cancellation of the nuclear-spin-independent effect by the NSD PNC effect is practically ruled out.

Finally, it may be noted that the next closest pair of hyperfine components of A and B is the $F=7.5$ pair for ^{161}Dy with a separation of 68.83(3) MHz [10]; here the NSD PNC is maximal. In addition, the anapole moment of the ^{161}Dy nucleus may be somewhat enhanced due to the close proximity of nuclear levels of opposite parity [5]. This makes this pair of components attractive for future NSD PNC experiments.

[1] C. S. Wood *et al.*, Science **275**, 1759 (1997).
[2] P. A. Vetter *et al.*, Phys. Rev. Lett. **74**, 2658 (1995).
[3] D. M. Meekhof *et al.*, Phys. Rev. Lett. **71**, 3442 (1993).
[4] M. J. D. Macpherson *et al.*, Phys. Rev. Lett. **67**, 2784 (1991).
[5] I. B. Khriplovich, *Parity Nonconservation in Atomic Phenomena* (Gordon and Breach, Philadelphia, 1991).
[6] W. C. Haxton, Science **275**, 1753 (1997).
[7] W. C. Martin, R. Zalubas, and L. Hagan, *Atomic Energy Levels—The Rare Earth Elements*, Natl. Bur. Stand. Ref. Data Ser., Natl. Bur. Stand. (U.S.), NBS-60 (U.S. GPO, Washington, DC, 1978).
[8] V. A. Dzuba, V. V. Flambaum, and I. B. Khriplovich, Z. Phys. D **1**, 243 (1986).
[9] V. A. Dzuba, V. V. Flambaum, and M. G. Kozlov, Phys. Rev. A **50**, 3812 (1994).
[10] D. Budker, D. DeMille, E. D. Commins, and M. S. Zolotorev, Phys. Rev. A **50**, 132 (1994).
[11] D. Budker, E. D. Commins, and D. DeMille, Opt. Lett. **16**, 1514 (1991).
[12] R. R. Lewis and W. L. Williams, Phys. Lett. **59B**, 70 (1975).
[13] R. W. Dunford, Ph.D. dissertation, University of Michigan, 1978 (unpublished), available from University Microfilms in Ann Arbor, MI.
[14] D. DeMille, D. Budker, E. Commins, and M. Zolotorev, in *Particle Astrophysics, Atomic Physics and Gravitation*, edited by J. Tran Thanh Van, G. Fontaine, and E. Hinds (Editions Frontières, Paris, 1994).
[15] I. I. Sobelman, *Atomic Spectra and Radiative Transitions* (Springer-Verlag, New York, 1992), p. 211.
[16] ELECTRO program by Integrated Engineering Software Inc., 1985.
[17] Magnetic Shield Corporation, Perfection Mica Co., Bensenville, IL 60106.
[18] J. B. Camp, T. W. Darling, and R. E. Brown, J. Appl. Phys. **69**, 7126 (1991).
[19] R. D. Barnard, *Thermoelectricity in Metals and Alloys* (Wiley, New York, 1972).
[20] W. Press, B. Flannery, S. Teukolsky, and W. Vettering, *Numerical Recipes in Fortran* (Cambridge University Press, Cambridge, 1986), p. 536.